

1 Supplemental material for the manuscript titled
2 **“Reconstruction of three-dimensional biventricular activation based on 12-lead ECG**
3 **via patient-specific modeling”**

4 by Pezzuto et al.
5

6 **ECG recordings**

7 The 12-lead ECG was recorded using a clinically available ECG machine (CS200 excellence,
8 Schiller AG) having a sampling rate of 1000/s and an amplitude resolution of 1.0 μV . The
9 target QRS complex was isolated from a single beat, with no additional filter applied. The
10 QRS onset and duration were detected manually. A linear detrend was subtracted from the
11 QRS complex to correct the baseline.

12 **Cardiac magnetic resonance**

13 Cardiac magnetic resonance (CMR) data were acquired with a 3T scanner (MAGNETOM
14 Skyra, Siemens Healthcare, Erlangen, Germany) with 36-channel torso coils. ECG-triggered,
15 steady-state free precession cine CMR were acquired in the 2-, 3- and 4-chamber orientation
16 and in a sequence of short-axis slices covering the ventricles (temporal resolution 25 to 40
17 ms, voxel size 1.2 mm \times 1.2 mm \times 8 mm.) A series of ultra-fast GRE sequences (axial,
18 coronal and sagittal) were obtained to describe the torso anatomy and the location of surface
19 electrodes. Scar detection was performed on a short-axis sequence 7 to 12 min after
20 gadolinium injection (gadobutrol, 0.2 mmol/kg body weight).

21 **Construction of the anatomical models**

22 Patient anatomies were semi-automatically reconstructed from the CMR images. Surfaces of
23 relevant anatomical structures were constructed from their contours using Blender (The
24 Blender Foundation). The outline of the ventricles was detected from short-axis cine images.
25 Atrial cavities, aorta, major veins and outflow tracts were traced from FLASH sequences.
26 Torso, lungs and electrode locations were segmented from an ultra-fast GRE dataset. Scarred
27 tissue was inferred from LGE-MRI sequence by manual contour and alignment. The cardiac
28 anatomy was eventually discretized into a 1-mm resolution grid. Ventricular fiber orientation
29 was assigned using a rule-based approach.¹ A 1-mm thick fast conducting layer was included
30 in both left and right ventricular endocardium.

31 Propagation model

32 The ventricular electrical activation $\tau(x)$ originated from selected locations, the early
33 activation sites (EASs), located at $x = s_i$ with onset of activation at time t_i , and spread across
34 the myocardium with given spatially-varying, direction-dependent conduction velocity
35 encoded in a tensor $\mathbf{D}(x)$. Mathematically, we modelled the activation with the eikonal
36 equation which reads

$$\begin{cases} \sqrt{\mathbf{D}(x) \nabla \tau \cdot \nabla \tau} = 1, \\ \tau(s_i) = t_i. \end{cases}$$

37 The conduction velocity tensor $\mathbf{D}(x)$ was set as

$$\mathbf{D} = \frac{\theta^2}{\beta} \mathbf{G}_{\text{in}} (\mathbf{G}_{\text{in}} + \mathbf{G}_{\text{ex}})^{-1} \mathbf{G}_{\text{ex}}$$

38 where β was the myocyte surface-to-volume ratio, $\theta = 2.1$, and \mathbf{G}_{in} and \mathbf{G}_{ex} were
39 respectively the intra- and extra-cellular electric conductivity. In order to mimic the Purkinje
40 network, a thin rapidly conducting layer was included along LV and RV endocardium, with a
41 different value of β . Scars (taken from CMR imaging) were modeled as non-conductive area,
42 with no border zone.

43 Lead fields computation and ECG formula

44 For the computation of the ECG we used the following formula:

$$V_k(t) = U' * w = \int_0^\infty U'(t - \xi) w_k(\xi) d\xi$$

45 The function $U(t)$ was the action potential as obtained from the Ten Tusscher-Panfilov ionic
46 model.² The function $w_k(t)$ represented the QRS complex obtained with the oblique dipole
47 layer formulation:³

$$w_k(t) = \int_{S(t)} \mathbf{G}_{\text{in}} \mathbf{n} \cdot \nabla Z_k d\sigma$$

48 where \mathbf{G}_{in} was the intracellular conductivity tensor, $S(t)$ the activation front with normal \mathbf{n}
49 pointing towards the depolarized region, and $Z_k(x)$ the lead field function for the lead
50 $k = 1, \dots, 12$. Each lead field function $Z_k(x)$ represented one of the 12 leads in the ECG.⁴

51 The formula for $V_k(t)$ can be easily derived from the reciprocity theorem applied to the
52 bidomain equation in the torso. According to this theorem, we have

$$V_k(t) = \int_{\Omega} \mathbf{G}_{\text{in}} \nabla V_m(x, t) \cdot \nabla Z_k(x) dx$$

53 where $V_m(x, t)$ is the transmembrane potential in the myocardial volume Ω . Using the

54 assumption $V_m(x, t) = U(t - \tau(x))$, the formula for the ECG follows from the computation
55 of the gradient and the application of the co-area formula.

56 **Identification of early activation sites**

57 The following parameters were considered in the optimization procedure: number N , location
58 s_i and onset t_i of the EASs; a global myocyte surface-to-volume ratio β ; a local scaling r_l of
59 the surface-to-volume ratio in 4 distinct regions (LV and RV myocardium, and LV and RV
60 fast endocardial layer). The total number of free parameters was therefore variable and
61 depending on the number of EASs. The initial value for β was 1000 cm^{-1} , while r_l was set to
62 unity. The other parameters for the eikonal model and the lead fields were set accordingly to
63 previous studies, being the same for all the patients.⁵

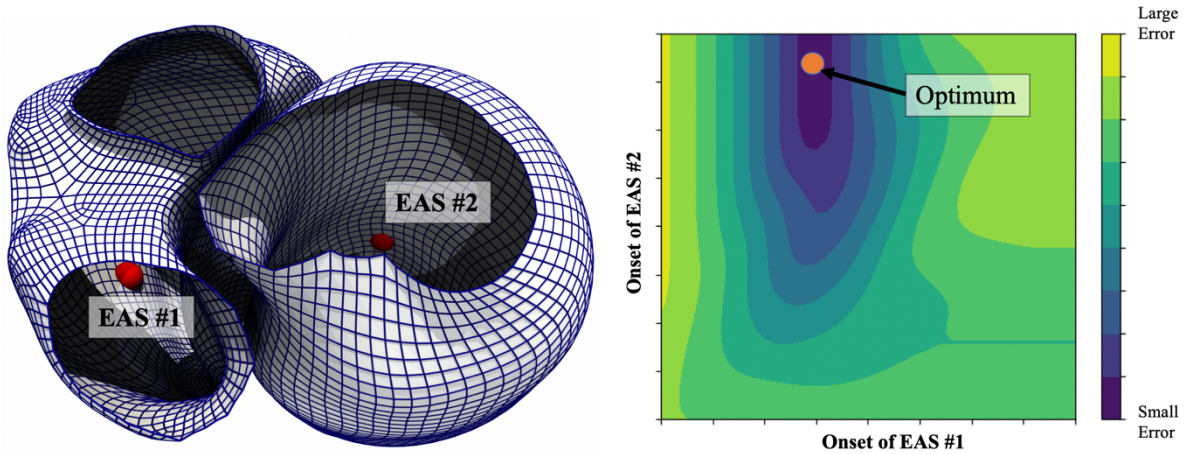
64 The first phase of the construction of the patient-specific models aimed at identifying an
65 optimal set of early activation sites (EASs) and a global CV. Given the activation map $\tau_i(x)$
66 at location x from each tentative EAS, we represented the combined activation map $\tau(x)$ at
67 location x in the following way:

$$\tau(x; t_1, \dots, t_n, \alpha, \beta) = \alpha \cdot \min\{\tau_1(x) + t_1, \dots, \tau_n(x) + t_n\} + \beta$$

68 for a set of unknown parameters $(t_1, \dots, t_n, \alpha, \beta)$, to be estimated. The formula for $\tau(x)$
69 represents the simultaneous activation of n EASs each activating at time $t = t_i$ and then
70 affinely transformed. We remark that $\tau(x)$ is still a solution of the eikonal equation, but its
71 evaluation only required a fraction of the total cost (only the ECG needs to be recomputed.)
72 The optimization of the free parameters to minimize the mismatch between recorded and
73 simulated ECG was achieved by iterating the following steps:

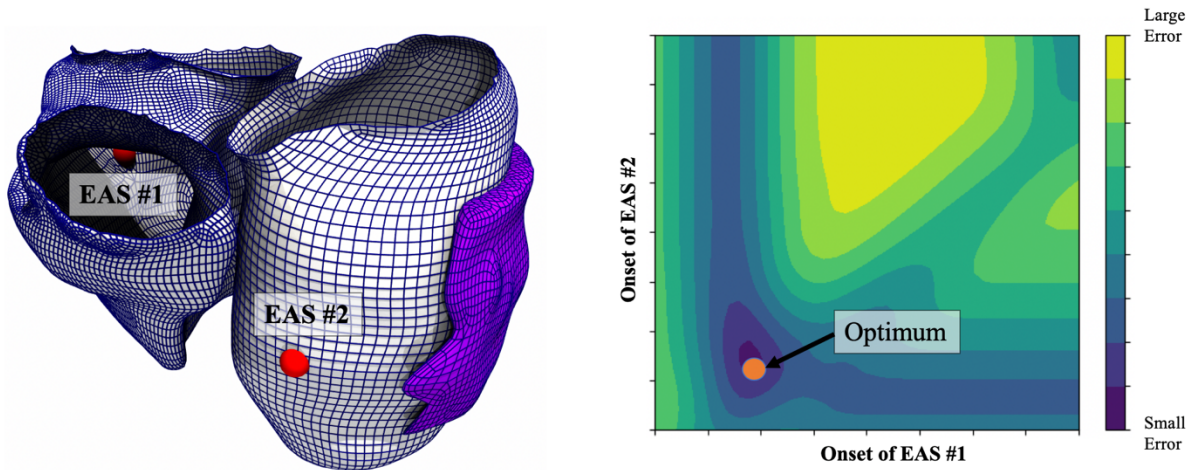
- 74 1. Optimize (t_1, t_2, \dots, t_n) for fixed n, α, β .
- 75 2. Optimize (α, β) for fixed n, t_1, \dots, t_n .
- 76 3. Remove EASs whose region of influence was small (below 1% of the total volume.)

77 For the optimization we used the BOBYQA algorithm.⁶ In the third step, we removed EASs
78 by setting $t_i = \infty$ in the combined activation map. In Figure 1 and Figure 2 we illustrate the
79 rationale of the first phase. All simulations were performed on a workstation equipped with
80 an NVIDIA GeForce GTX-1080 card.



81

82 *Figure 1. Illustrative example of the first optimization phase. We consider only 2 EASs, one placed on the RV endocardium,*
 83 *the other on the LV endocardium. We then evaluated the error between recorded and simulated ECG for several*
 84 *combinations of onsets (right plot). The optimal error (here unique) is for very late activation of EAS #2 and early activation*
 85 *of EAS #1, probably indicating a left bundle branch block.*



86

87 *Figure 2. Illustrative example of the first optimization phase for a patient with scar and without a bundle branch block. The*
 88 *procedure is as the previous figure. In this case, the optimal onset indicates that both points activate early.*

89 **Parametrization of endocardial surface and bull's-eye plot**

90 Segmented LV and RV endocardium were parametrized with a global coordinate system to
 91 facilitate the localization of EASs and the visualization of endocardial activation (bull's-eye
 92 plots). Every 3-D point of the surface with canonical coordinates (x, y, z) was mapped to 2-D
 93 “texture” coordinates (u, v) within a circle of unit radius. In this way, the possibly complex
 94 endocardial surface was represented by the unit circle. An EAS on the surface was similarly
 95 mapped onto the unit circle.

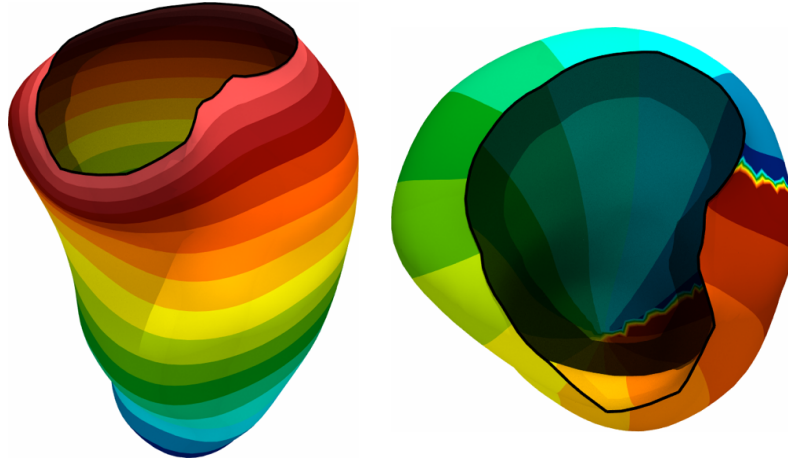


Figure 3. Example of the parametrization of the LV endocardium. On the left, the radial coordinate in the texture space, that is $u^2 + v^2$, on the right the rotational coordinate.

96

97 The parametrization was based on a previously proposed method, with minor modifications.⁷

98 In our case, we only parametrized the endocardial surfaces and not the whole myocardium.

99 We automatically identified the outer boundary of the surface (the valve ring) and mapped

100 this curve to the unit circumference, with $u = \cos(2\pi s)$ and $v = \sin(2\pi s)$, being s the

101 curvilinear coordinate of the boundary. Then, we harmonically extended the boundary data to

102 the whole surface, that is $\nabla^2 u = 0$ and $\nabla^2 v = 0$ with the above boundary data. This

103 parametrization is generally not uniform across the surface, in the sense that an infinitesimal

104 square in the texture space is typically mapped to a larger square when it is close to the apex

105 rather than close to the base. Therefore, we recomputed the parametrization by solving the

106 problem

107
$$\nabla \cdot (\mathbf{G}^{-1} \nabla w) = 0, G = \begin{pmatrix} \frac{\partial X}{\partial u} \\ \frac{\partial X}{\partial v} \end{pmatrix}^T \begin{pmatrix} \frac{\partial X}{\partial u} \\ \frac{\partial X}{\partial v} \end{pmatrix}, X = [x, y, z]^T \text{ and } w = [u, v]^T.$$

108 The bull's-eye plot was defined as the representation of the LV endocardial surface in the

109 texture space, since $u^2 + v^2 \leq 1$. This may slightly differ from other bull's-eye

110 representations, which are generally based on a projection onto a prolate spheroid aligned

111 with the LV.

112 **Interpolation of recorded activation map**

113 In the LV and RV endocardium, a radial basis function regression method with multiquadric

114 functions was employed to interpolate the recorded activation map in the full surface from

115 acquired locations.

116 Robustness of validation

117 In the recorded data, an uncertainty in the spatial location of electro-anatomic mapping
118 (EAM) points (2 mm) and in the detected activation time (4 ms) was assumed. With a Monte
119 Carlo approach (10'000 samples) we perturbed the recorded EAM points with Gaussian noise
120 using the above variances and repeated the evaluation of breakthrough-point (BP) location.
121 Below we report the distribution of localization error for patient #1 in the case of BP
122 evaluated as the barycenter of the earliest activated region (10% of total activation), versus
123 the case when BP is simply the earliest activated point of the mesh. This analysis showed that

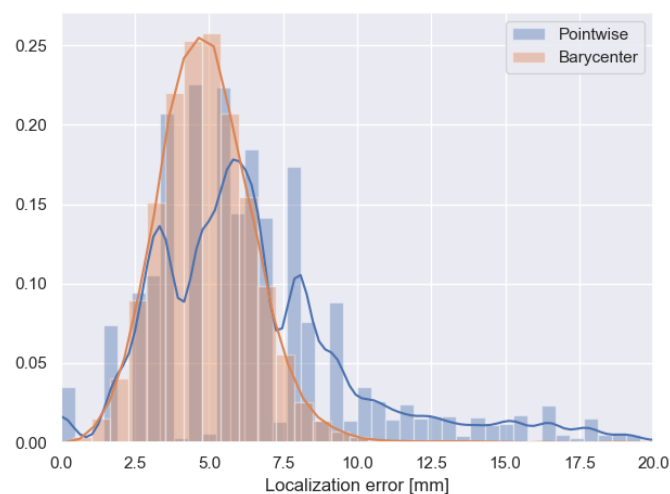


Figure 4. Distribution of localization error of BP with two different methods to identify the BP.

124 our definition of BP (and LAP) is more robust to uncertainty.

125 References

- 126 1. Potse M, Krause D, Kroon W, Murzilli R, Muzzarelli S, Regoli F, *et al.* Patient-
127 specific modelling of cardiac electrophysiology in heart-failure patients. *Europace*
128 2014;**16**:iv56–61.
- 129 2. Ten Tusscher KHWJ, Panfilov AV. Alternans and spiral breakup in a human
130 ventricular tissue model. *Am J Physiol Circ Physiol* 2006;**291**:H1088–100.
- 131 3. Colli Franzone P, Pavarino LF, Scacchi S. Mathematical Cardiac Electrophysiology.
132 Cham: Springer International Publishing; 2014.
- 133 4. Potse M. Scalable and Accurate ECG Simulation for Reaction-Diffusion Models of the
134 Human Heart. *Front Physiol* 2018;**9**.
- 135 5. Pezzuto S, Kal’avský P, Potse M, Prinzen FW, Auricchio A, Krause R. Evaluation of a

- 136 Rapid Anisotropic Model for ECG Simulation. *Front Physiol* 2017;**8**:265.
- 137 6. Powell MJD. The BOBYQA algorithm for bound constrained optimization without
138 derivatives. Dep. Appl. Math. Theor. Physics, Cent. Math. Sci. Wilberforce Road,
139 Cambridge CB3 0WA, England. 2009.
- 140 7. Bayer J, Prassl AJ, Pashaei A, Gomez JF, Frontera A, Neic A, *et al.* Universal
141 ventricular coordinates: A generic framework for describing position within the heart
142 and transferring data. *Med Image Anal Elsevier*; 2018;**45**:83–93.
- 143